TOSHKENT DAVLAT TRANSPORT UNIVERSITETI
Tashkent state transport university

Issue 2, 2025

INTERNATIONAL JOURNAL OF TRANSPORT AND TECHNOLOGICAL MACHINES

ISSN: 3030-363X



THE SCIENCE OF TODAY IS THE TECHNOLOGY OF TOMORROW

INTERNATIONAL JOURNAL OF TRANSPORT AND TECHNOLOGICAL MACHINES

Published since 2024

Editorial Council:
Mukhitdinov A.A., Ziyayev K.Z., Rustamov K.J, Abdurazzakov U.
Editorial team:
Chief Editor – Rustamova K.J.
Deputy Chief Editor – Rustamova N.R.

Members of the editorial board:
Mukhitdinov A.A., Ziyayev K.Z., Rustamov K.J., Abdurazzoqov U.A., Saman M. Almufti., Habibollah Haron., Gai-ge Wang., Jayson A. Dela Fuente., Ahmad A. AlRabab'ah., Rami Hikmat Fouad AL-Hadeethi., Emad Kamil Hussein., Ayman Abu-Rumman.

TASHKENT STATE TRANSPORT UNIVERSITY

Founder of the scientific and technical journal, “International Journal of Transport and Technological Machines” – Tashkent State Transport University (100167, Republic of Uzbekistan, Tashkent, Temiryulchilar str., house No. 1, office: 379, tel Tel.: +998 97 156 94 21 E-mail: k.j.rustamov82@gmail.com).

In the International Journal of Transport and Technological Machines publishes the most significant results of scientific and applied research carried out in universities of transport and information technology profile, other higher educational institutions, research institutes and centers of the Republic of Uzbekistan and foreign countries.

The journal is published 4 times a year and contains publications in the following main areas:

- Automotive engineering
- Civil Engineering
- Construction Engineering and Management
- Instrumentation technology
- Environmental Engineering
- Environmental Sciences
- Green production
- Industrial Safety
- Mechanical Engineering Technology
- Mining
- Mechatronics

CONTENTS

1. Khankelov T.K., Politaeva N.A., Atabaev G‘.G‘., Choriev A.Sh. JUSTIFICATION OF THE OPTIMUM COMBINATION OF PARAMETERS OF SPECIALIZED PLOWS FOR THE SHANTUI SD 32 BULLDOZER WHEN MOVEMENT OF LOW-DENSITY MATERIALS…….....4

2. Bakhytzhan Kedelbaev., Dmitriy Ayrapetov., Ismailov Ergash. ANALYSIS OF THE OPERATIONAL CHARACTERISTICS OF ENGINE OILS IN GASIFIED DIESEL ENGINES …….17

3. Tursunov M. N., Sabirov H., Axtamov T. Z., Sh. A. Abriyev. EXPERIMENTAL EVALUATION OF THE THERMAL EFFICIENCY OF A MOBILE WATER DESALINATION DEVICE……....25

TOSHKENT DAVLAT TRANSPORT UNIVERSITETI
Tashkent state transport university
International Journal Of Transport And Technological Machines
Tashkent 2025, issue 2, https://ijttm.uz/

JUSTIFICATION OF THE OPTIMAL COMBINATION OF PARAMETERS FOR SPECIALIZED BULLDOZER BLADES FOR THE SHANTUI SD32 WHEN HANDLING LOW-DENSITY MATERIALS

Khankelov T.K.[1], Politaeva N.A.[2], Atabaev G‘.G‘.[1], Choriev A.Sh.[1]

[1]Tashkent State Transport University, Uzbekistan

[2]Peter the Great St. Petersburg Polytechnic University, Russia

Abstract: The article is devoted to finding the optimal combination of parameters of spherical and “landfill” dumps intended for the SHANTUI SD 32 bulldozer. Mathematical modeling of the bulldozer’s working process when moving low-density materials was adopted as a research method; the technical performance of the bulldozer was selected, providing a reliable assessment of the results of the parametric synthesis of dumps. To develop analytical relationships for the technical productivity of a bulldozer, the process of prism formation is divided into three discrete phases and the dependence of the technical productivity of a bulldozer for each phase is determined, taking into account losses from the drawing prism.

The optimal dimensions of a box blade for equipping the SHANTUI SD32 bulldozer are: working width up to 3730 mm, radius of curvature up to 1700 mm, cutting edge width up to 460 mm, canopy width up to 140 mm, opening length up to 860 mm. The optimal dimensions of the “landfill” blade for equipping the SHANTUI SD32 bulldozer are: working width up to 3900 mm, radius of curvature up to 460 mm, cutting edge width up to 124 mm, canopy width up to 610 mm.

Key words: drawing prism, phase, loss, technical performance, box dump, “landfill” dump.

1. Introduction

Bulldozers are widely used in construction. Currently, their numbers are nearly equal to those of excavators. Bulldozers account for approximately 35-40% of all earthmoving work in construction. They are used in road construction, land reclamation, irrigation projects, and mining quarries. Bulldozers perform grading work, construct highway and railway embankments using side borrow pits, transport soil over distances up to 100 meters, dig canals and foundation pits, backfill trenches and holes, clear roads and construction sites of snow, fell trees and uproot stumps. They are also used as pusher vehicles when working with scrapers [1].

It is known that certain materials (snow, wood chips, coal, etc.) are in some cases most efficiently moved by bulldozers. However, the capacity of standard blades designed for soil handling does not allow full utilization of the machine's traction and power in such cases. For these situations, high-capacity bulldozer blades, referred to here as specialized blades, have been developed.

Within the scope of this study, the term "specialized blades" refers to high-capacity bulldozer blades for which large-scale earthmoving is not the sole, primary, or preferred application. These include [2]:

- **Spherical blades** – for moving lightweight materials,
- **Box blades** – for handling lightweight, loose, liquefied, and coarse-fragment materials,
- **Landfill blades** – for moving municipal waste.

This study focuses on determining the optimal combination of parameters for such blades on the **SHANTUI SD32 bulldozer**. The research method employed is **mathematical modeling of the bulldozer's working process**, with **technical productivity** serving as the criterion for evaluating blade parameters, ensuring a reliable assessment of parametric blade synthesis results [3].

2. Literature Review and Problem Statement

Bulldozer productivity is influenced by numerous factors, including design, operational, and ergonomic aspects. Additionally, some researchers consider that maximum soil accumulation in front of the blade, its contact area with the blade surface, and the blade's cross-sectional adaptation to the natural soil chip formation trajectory also play a role [4].

For example, studies [5,6] examine how blade design and material properties affect productivity, with soil loss from the accumulation prism accounted for only through a loss coefficient. Research [7,8] incorporates both design and operational parameters in productivity calculations. Notably, some studies [9,10] also factor in operator skill by applying a correction coefficient. Works [11,12] focus on calculating key parameters for earthmoving machinery.
Studies [13,14] have examined how the properties of processed materials affect the efficiency of excavation, leveling, and transportation operations. Currently, numerous research efforts focus on automating work processes, developing unmanned control systems for earthmoving equipment, and evaluating how autonomous operation impacts machine performance.

Despite extensive research on bulldozer productivity assessment, two key challenges remain particularly relevant:

1) Material loss quantification from the drag prism during transportation
2) Optimal blade selection based on the specific properties of handled materials

3. Research Purpose and Objectives

Among the generalized performance indicators for construction machinery that mainly consider energy and mass characteristics, productivity occupies a special place. Evaluating productivity allows assessing how well a machine fits its functional purpose.

The study aims to find the optimal combination of parameters for box-type and "landfill" blades for the SHANTUI SD32 bulldozer to achieve maximum technical productivity when handling low-density, low-cohesion materials.

To achieve this goal, the following tasks were addressed:

- Developing a mathematical model of bulldozer productivity equipped with any blade type, accounting for material losses from the drag prism;
- Determining the material parameters that the blades are designed to handle;
- Classifying and quantitatively describing probable operational scenarios;
- Developing recommendations for optimal parameter combinations of box-type and "landfill" blades for the SHANTUI SD32 bulldozer.

4. Materials and Methods

The transported material can either be stockpiled or distributed as a layer on the supporting surface.

When moving a material pile (windrow), losses begin when the entire volume of material captured by the blade starts moving across the supporting surface - that is, when the drag prism formation is complete. In this case:

$$Q = Q_{max} \quad (1)$$

Where - Volume of the drawing prism, м^3; Q_{max}- Maximum value of the drawing prism volume, м^3.

Current drawing prism volume

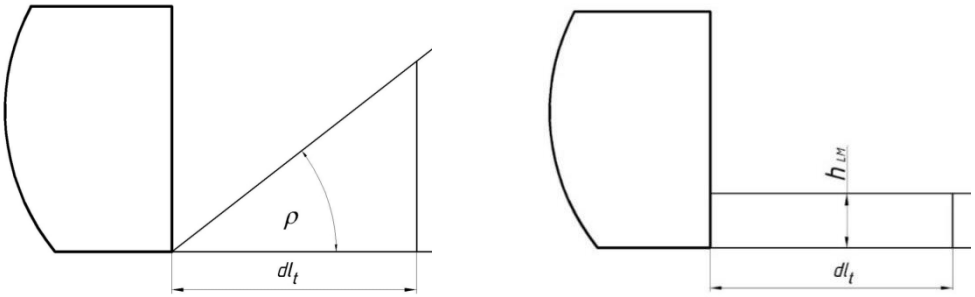
$$Q_i = Q_{i-1} + dQ, \quad (2)$$

where Q_i- Drawing prism volume Q at the end of the -th section of the bulldozer path with a length of dl_t, м^3; Q_{i-1}-drawing prism volume Q at the beginning of the i-th section of the bulldozer path with a length of dl_t, м^3; dQ-volume of loosened material entering the drag prism at the i-th section of the bulldozer's path with a length of dl_t, м^3.

$$dQ = (i - 0{,}5) \cdot dl_t^2 \cdot tg\rho \cdot L \cdot f_r, \quad (рис.3), \quad (3)$$

where dl_t- l - bulldozer's incremental step length, m; - material's angle of repose, deg;

L – blade cutting width, m; f_r- material loosening coefficient. The volume of material entering the drag prism is shown in Fig. 1.



a) b)

Fig. 1. Material volume entering the drag prism: a) when collecting from a pile; b) during layer-by-layer cutting.

where ρ-angle of repose of the material, degrees; dl_t-length of the bulldozer's path increment step, mm; h_{LM}-thickness of material layer cut by the blade, mm.

When forming the drag prism from a material layer, it is assumed that the process occurs in three phases (Fig. 2):

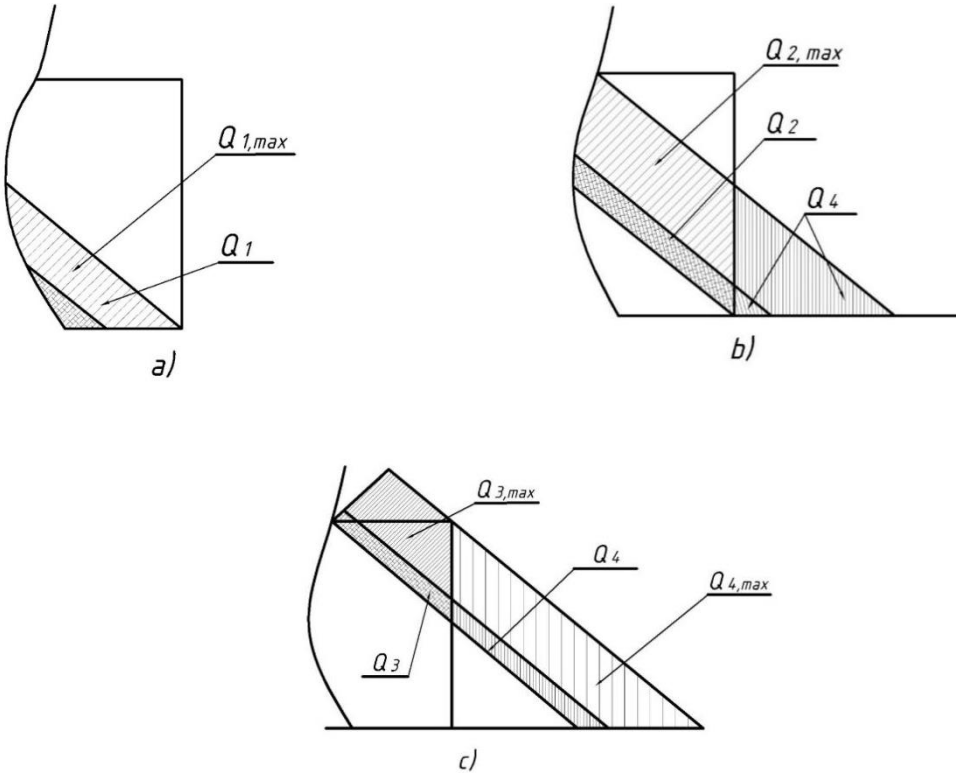


Fig. 2. Phases of drag prism formation: a) first phase; b) second phase; c) third phase

Phase 1 - the drag prism grows from zero to volume $Q_{1,max}$ due to the growth of the component Q_1 (Fig. 2a); no losses occur from the drag prism;

Phase 2 - the drag prism grows from volume $Q_{1,max}$ to volume $(Q_{1,max} + Q_{2,max} + Q_4)$ due to the growth of components Q_2 and Q_4 (fig.2, b); loss volume is proportional to volume Q_4;

Phase 3 - the drag prism grows from volume $(Q_{1,max} + Q_{2,max} + Q_4)$to volume $(Q_{1,max} + Q_{2,max} + Q_{3,max} + Q_{4,max})$ due to the growth of components Q_3 and Q_4 (fig.2, v); volume of losses is proportional to volume Q_4;

where Q_1, Q_2, Q_3, Q_4-components of the drag prism, m³; $Q_{1,max}, Q_{2,max}, Q_{3,max}, Q_{4,max}$-maximum values of volumes, corresponding to volumes Q_1 Q_2, Q_3, Q_4.

The phase ends when the drag prism stops growing. For the current volume value Q of the drag prism, the following holds true:

$$Q_i = Q_{i-1} + dQ - Q_L, \quad (4)$$

(fig.2,b): Q_L-volume of losses at the m-th section of the bulldozer's path with length dl_t, м^3.

$$dQ = h_{LM} \cdot L \cdot dl_t \cdot f_r . \quad (5)$$

where f_r- material loosening coefficient.

The proportionality of losses to the volume of the drag prism portion not laterally confined by the blade's wings (volume Q_4 in fig..2), is expressed by the formula:

$$Q_L = Q_4 \cdot K_L \cdot dl_t, \quad (6)$$

where K_L- coefficient of losses from the drag prism.

Thus, the problem of accounting for losses from the drag prism when calculating its volume reduces to determining the volume Q_4 on discrete sections of the bulldozer's path from the start point of prism formation to its completion point. Along this path, the nature of the volume formation process will change at points (Fig. 2) corresponding to the following boundary conditions:

$Q_1 = Q_{1,max}$ -start of the volume formation process Q_4 (volume Q_4 begins to form as soon as the volume Q_1 reaches its maximum value); (7)

$Q_2 = Q_{2,max}$ - change in the nature of volume formation Q_4 (nature of volume formation Q_4 changes as soon as the volume Q_2 reaches its maximum value); (8)

$Q_3 = Q_{3,max}$ - completion of the drag prism growth process (the drag prism growth will stop as soon as the volume Q_3 reaches its maximum value); (9)

Another condition for stopping the growth of the drag prism is the equality between losses and the volume of material entering the blade:

$$Q_L = dQ, \quad (10)$$

Moreover, condition (10) takes priority over condition (9), since when it occurs, the growth of the drag prism stops, even if the volume Q_3 has not yet reached its maximum value.

4.1. Volume of the drag prism accounting for losses

4.2. According to the adopted assumptions and their corresponding boundary conditions (7)...(10) for calculating volumes Q_1, $Q_{1,max}$, Q_2, $Q_{2,max}$, Q_3, $Q_{3,max}$, Q_4 and $Q_{4,max}$4.2. Calculation schemes shown in Figures 3-8 were adopted. To simplify the analysis, the cylindrical surfaces of the blade sections were replaced with vertical planes. When finally determining the drag prism volume, the introduced error is corrected by adding to the prism a volume proportional to the segment formed by the blade surface and vertical plane (Fig. 5).

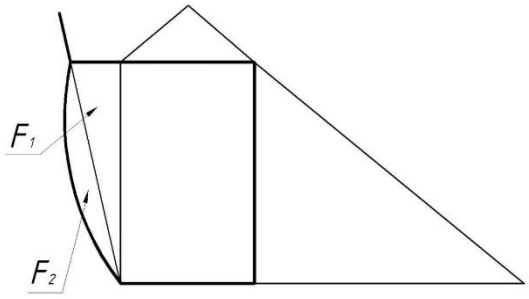


Fig. 3. Additional volume formed by the curvature of the blade and its inclination at the cutting angle.

$$Q_{me} = (F_1 + F_2)[L + 2W(1 - cos\mu)], \quad (11)$$

$$F_1 = 0{,}5R^2(\alpha - sin\alpha), \quad (12)$$

$$F_2 = \frac{H}{2}\sqrt{[2(1 - cos\alpha) + k_a^2 + 2k_a \cdot sin\alpha]R^2 - H_0^2}, \quad (13)$$

$$H_0 = \frac{H}{[1+k_b \cdot \sin(\alpha+\gamma+\delta)]}. \quad (14)$$

where F_1, F_2-areas of cross-sections of cylindrical segments, м^2; R-radius of curvature of the cross-sectional profile of the blade, m; -height of the blade with a visor, m; k_α-ratio of the cutting edge width to the radius of curvature; k_b--ratio of the visor width to the radius of curvature;

H_0-height of the blade without a visor, m.

Verification of condition (7) involves calculating the maximum volume value (Fig. 4).

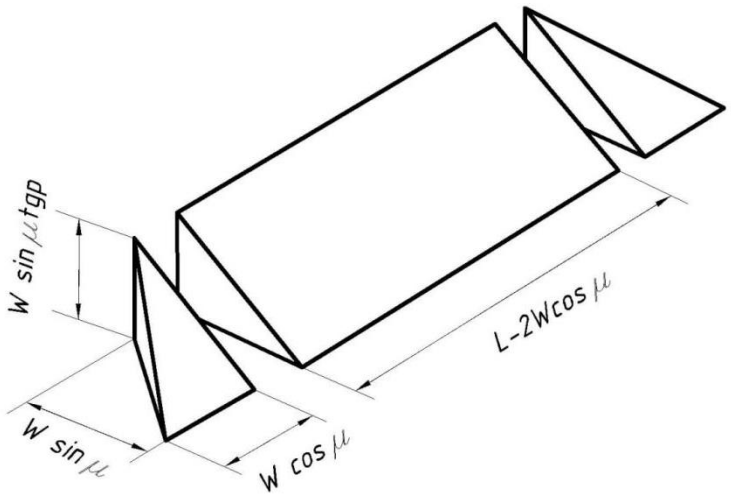


Fig. 4. Diagram for calculating the volume of the drawing prism at the end of the 1st phase of its growth.

$$Q_{1,max} = W^2 \sin^2\mu \cdot tg\rho \left[\frac{L-2W\cos\mu}{2} + \frac{2W\sin\mu}{3}\right], \quad (15)$$

In the second phase of blade filling, the drawing prism grows due to volumes and related ratios:

$$Q_{2,i} + Q_{4,i} = Q_{2,(i-1)} + Q_{4,(i-1)} + dQ, \quad (16)$$

from which it follows: $dQ_2 + dQ_4 = dQ$, (17)

where

$$dQ_2 = Q_{2,i} - Q_{2,(i-1)}, \quad (18)$$

$$dQ_4 = Q_{4,i} - Q_{4,(i-1)}, \quad (19)$$

From the calculation scheme (Fig. 4):

$$dQ_2 = W\sin\mu(L - W\cos\mu)dz_2, \quad (20)$$

$$dQ_4 = dz_2\left[z_2 \cdot \frac{L}{tg\rho} + L \cdot \frac{dz_2}{2tg\rho}\right], \quad (21)$$

Where

$$dz_2 = \left[-c_2 + \sqrt{(c_2^2 + 4b_2 dQ)}\right]/2b_2, \quad (22)$$

$$b_2 = \frac{L}{2tg\rho}, \quad (23)$$

$$c_2 = (L - W\cos\mu)W\sin\mu + \frac{z_2 L}{tg\rho}, \quad (24)$$

$$z_{2,i} = z_{2,(i-1)} + dz_2. \quad (25)$$

where dz_2-projection of layer thickness dQ_2 onto the vertical axis OZ; z_2-projection of layer thickness $Q2$ onto the vertical axis OZ.

Volumes Q_2 and Q_4 are calculated using formulas

$$Q_{2i} = Q_{2(i-1)} + dQ_2, \quad (26)$$

$$Q_{4,i} = Q_{4(i-1)} + dQ_4, \quad (27)$$

With the verification of the condition

$$Q_2 \le Q_{2,max}, \quad (28)$$

Where $Q_{2,max} = (H - Wsin\mu tg\rho)Wsin\mu(L - Wcos\mu)$, (29)

In the third phase of blade filling, the drawing prism increases due to volumes Q_3 and Q_4 (fig..2, c), related to the ratio

$$Q_{3,i} + Q_{4,i} = Q_{3(i-1)} + Q_{4(i-1)} + dQ, \quad (30)$$

from which it follows $dQ_3 + dQ_4 = dQ$, (31)

Where

$$dQ_3 = Q_{3,i} - Q_{3(i-1)}, \quad (32)$$

$$dQ_4 = Q_{4,i} - Q_{4(i-1)}, \quad (33)$$

The calculation scheme for volumes determining the growth of drawing prisms in the second and third phases is shown in Figures 5 and 6.

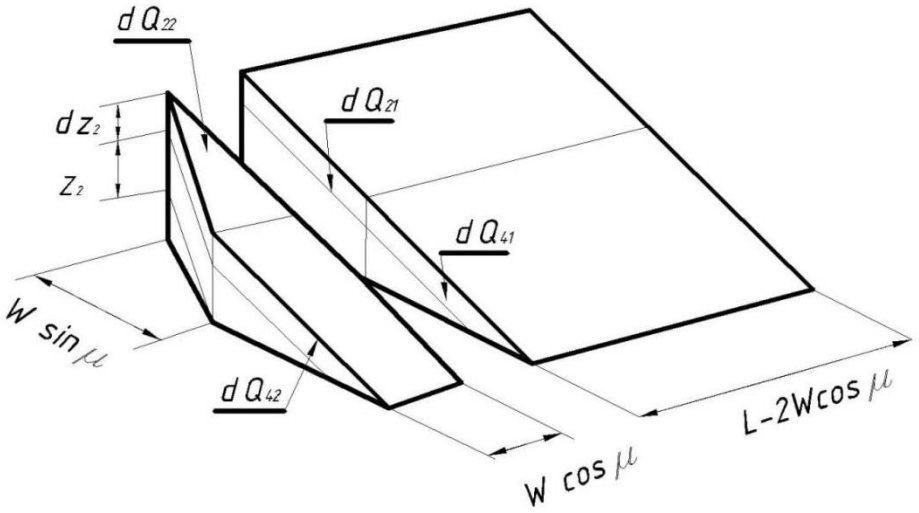


Fig. 5. Diagram for calculating volumes determining the growth of the drawing prism in the second phase

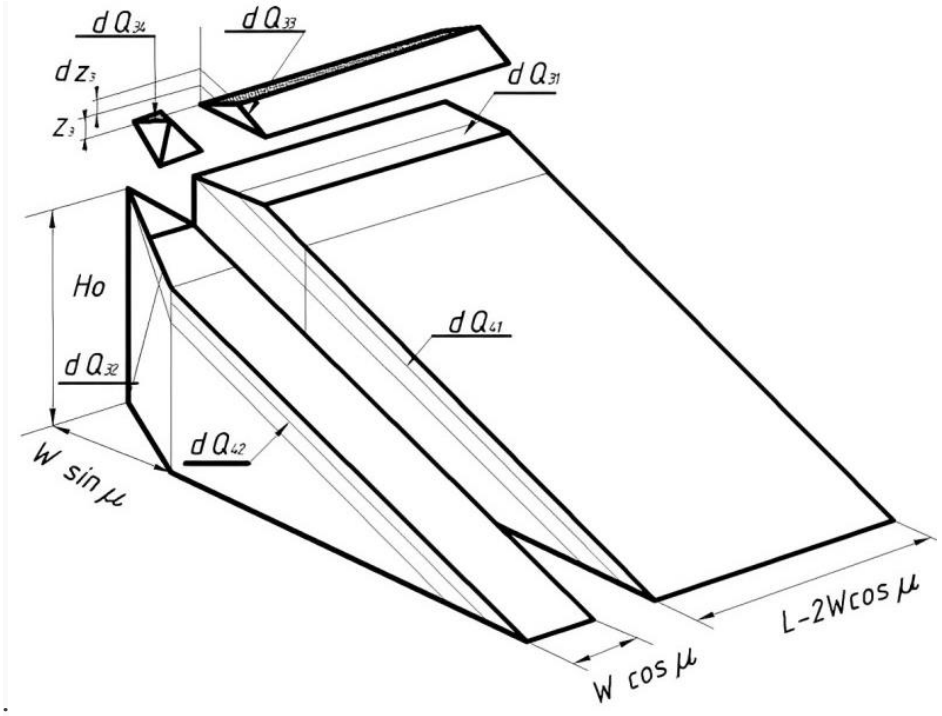


Fig. 6. Diagram for calculating volumes determining the growth of the drawing prism in the third phase.

From the calculation scheme in Fig. 6, it follows that

$$dQ_3 = a_3 dz_3^3 + \left[b_3 - \frac{L}{2tg\rho}\right] dz_3^2 + [c_3 - \frac{L(z_2+z_3)}{tg\rho}]dz_3, \quad (34)$$

$$dQ_4 = \left[\frac{L}{2tg\rho}\right] dz_3^2 + \left[\frac{L(z_2+z_3)}{tg\rho}\right] dz_3. \quad (35)$$

Magnitude dz_3 is found from the equation

$$a_3 dz_3^3 + b_3 dz_3^2 + c_3 dz_3 = dQ, \quad (36)$$

where

$$a_3 = -1/(6tg^2\rho tg\mu), \quad (37)$$

$$b_3 = \frac{z_3}{2tg^2\rho tg\mu} + \frac{(L-2Wcos\mu)z_3}{2tg\rho} + L/(2tg\rho), \quad (38)$$

$$c_3 = \frac{z_3^2}{2tg^2\rho tg\mu} + \frac{(L-2Wcos\mu)z_3}{2tg\rho} + (L-2Wcos\mu)Wsin\mu + L(z_2+z_3)/tg\rho, \quad (39)$$

$$z_{3,i} = z_{3(i-1)} + dz_3, \quad (40)$$

Volumes Q_3 and Q_4 are calculated using formulas

$$Q_{3,i} = Q_{3(i-1)} + dQ_3, \quad (41)$$

$$Q_{4,i} = Q_{4(i-1)} + dQ_4, \quad (42)$$

with the verification of conditions

$$Q_3 \le Q_{3,max} \text{ and } Q_4 \le Q_{4,max}, \quad (43)$$

where

$$Q_{3,max} = (Wsin^2\mu)tg\rho(3L - 4Wcos\mu)/4, \quad (44)$$

$$Q_{4,max} = \frac{H_0^2 L}{2tg\rho}, \quad (45)$$

For the path traveled by the blade, at any point it is equal to

$$l_{t,i} = l_{t,(i-1)} + dl_t, \quad (46)$$

4.2. Nomenclature and Characteristics of Transported Materials

According to the technical assignment, the materials intended to be handled by the specialized dumps include: freshly fallen snow, compacted and packed snow, solid household waste, liquefied soil, loam, hard coal, and wood chips. The physical properties of these materials, which characterize them as transported media and supporting surfaces, have been determined through analysis of literary sources and are summarized in Table 1.

Table 1

Physical properties of materials

Properties of materials	*Material number**							
	1	*2*	*3*	*4*	*5*	*6*	*7*	*8*
*Cohesion index***	*1*	*1*	*1*	*1*	*2*	*1*	*2*	*1*
Coefficients:								
Friction on metal	*0,08*	*0,06*	*0,06*	*0,55*	*0,13*	*0,50*	*0,45*	*0,4*
Friction on material	*0,46*	*0,51*	*0,57*	*1,00*	*0,18*	*0,50*	*0,75*	*1,05*
Material loosening	*1,0*	*1,2*	*1,2*	*1,4*	*1,0*	*1,1*	*1,0*	*1.2*
Resistance to movement	*0,12*	*0,1*	*0,1*	*0,12*	*0,1*	*0,1*	*0,12*	*0,12*
N.A. Ulyanova	*0,05*	*0,05*	*0,05*	*0,05*	*0,05*	*0,05*	*0,05*	*0,05*
a_u								
b_u	*1,76*	*1,76*	*1,76*	*1,76*	*1,76*	*1,76*	*1,76*	*1.76*
n	*12*	*12*	*14*	*8*	*12*	*3*	*6*	*8*
Cutting resistance, кН/м²	*5,1*	*21,6*	*31,5*	*20,0*	*17,8*	*108*	*20,0*	*30,0*
Angle of repose, deg	*36*	*60*	*60*	*55*	*10*	*40*	*37*	*50*
Bulk density, м/м³	*0,3*	*0,40*	*0,05*	*0,43*	*1,8*	*1,8*	*0,8*	*0,35*

*1 - freshly fallen snow, 2 - compacted snow, 3 - rolled snow, 4 - municipal solid waste, 5 - liquefied soil, 6 - loam, 7 - bituminous coal, 8 - wood chips.

**1 - cohesive material, 2 - non-cohesive material.

Conclusion

The analysis of the effectiveness of equipping the SHANTUI SD32 bulldozer with high-capacity specialized blades showed that the bulldozer can achieve maximum productivity when working with materials that differ in their characteristics from ordinary loam (snow, municipal waste, liquefied soil, bituminous coal, wood chips) by using box and landfill blades.

The feasibility of using one of them depends on the probability of the bulldozer working on liquefied soil (or similar material) versus other materials (snow, waste, coal, wood chips).

The undeniable effectiveness of equipping the bulldozer with a box blade is expected when the probability of the machine working on liquefied soil (or similar material) is 0.5 or higher.

Optimal dimensions of the box blade for the SHANTUI SD32 bulldozer:

Cutting width: up to 3730 mm

Curvature radius: up to 1700 mm

Cutting edge width: up to 460 mm

Canopy width: up to 140 mm

Wing length: up to 860 mm

Optimal dimensions of the landfill blade for the SHANTUI SD32 bulldozer:

Cutting width: up to 3900 mm

Curvature radius: up to 460 mm

Cutting edge width: up to 124 mm

Canopy width: up to 610 mm

References

1. Баловнев В.И., Глаголев С.Н., Данилов Р.Г., Кустарев Г.В., Шестопалов К.К., Герасимов М.Д. Машины для земляных работ: конструкция, расчет, потребительские свойства: Изд-во БГТУ, 2012.-401с. Доступно по адресу: https://adarka.ru/knigi/traktory-i-spetstekhnika/1899/

2. Mikhail Dudkin, Alina Kim, Bekzat Aukenova, Radoslav Radenkov, Andrey Saveliev, Nikita Andryukhov. (2022).Theoretical investigations of the process of interaction with

envioronment of a bulldozer bladow with variable geometry. Journal of Applied Engineering Science.20,798-807.DOI: http://doi.org/10.5937/jaes0-37210

3. Narqul Aslanov, Khusniddin Irisov. Mathematical model of resistance to spreading forces using a bulldozer blade.E3S Web of Conf.390,01032, 1-5 (2023). DOI: http://doi.org/10.1051/e3sconf/202339001032

4. Сурашов Н.Т., Асматуллаев Р.Б., Толымбек Д.Н. Определение рациональной формы отвала бульдозера с учетом грунтового фона Республики Казахстан. «Вестник СибАДИ».2021; 18(6): 662-677.DOI: https://doi.org/10.26518/2071-7296-2021-18-6-662-677

5. Хмара Л.А.Научное сопровождение строительных и дорожных машин: исследование, расчет, создание, выбор, использование.Вестник Преднепровской государственной академии строительства и архитектуры.2015, №7-8 (209).ISSN 2312-2676. с.48-69. Доступно по адресу: https://oaji.net/articles/2015/2528-1447325684.pdf

6. Ракша С.В., Главацкий К.И.,Гребенко Ю.О.Исследование процесса копания грунта физической моделью бульдозерного оборудования с неповоротным отвалом и сменной ножевой системой. Вестник Харьковского национального автомобильно-дорожного университета. Вып.88, 2020, том.II.с.86-92. Доступно по адресу: https://cyberleninka.ru/article/n/doslidzhennya-protsesu-kopannya-gruntu-fizichnoyu-modellyu-buldozernogo-obladnannya-z-nepovorotnim-vidvalom-ta-zminnoyu/viewer

7. Jaroslaw Selech, Dariusz Ulbrich, Konrad Wlodarczyk, Zaneta Staszak, Jacek Marcinkiewicz, Dawid Ramek, and Bartosz Baran. A working desing of a bulldozer blade as additional equipment of a compaction drum roller. MATEC Web of Conferences 254, 04005 (2019). DOI: https://doi.org/10.1051/matecconf/201925404005

8. Nada Barakat, Deepak Sharma.Evolutionary multi-objective optimization for bulldozer and its blade in soil cutting. International Journal of Management Science and Engineering Management. Доступ по адресу: https://www.iitg.ac.in/dsharma/papers/journal/2019multiOBJ bulldozer.pdf.

9. Tavbay Khankelov, Tulkun Askarhoodzaev, Norkul Aslanov.Modeling of segmental excavator working tool for soil compaction.(2023).E3S Web of Conferences 401(826).DOI: https://doi.org/10.1051/e3sconf/202340102052.

10. Masami Hirayama, Jose Guivant, Jayanta Katupitiya, Mark Whitty. Path planning for autonomous bulldozer. Mechatronics. Volume 58, 2019, pp.20-38. DOI: http://doi.org/10.1016/j.mechatronics.2019.01.001

11. Sang-Ho Kim, Yong-Seok Lee, Dong-Ik Sun, Sang-Keun Lee, Bo-Hyun Yu, Sung-Hoon Jang, Wansoo Kim, Chang-Soo Han. Development of bulldozer sensor system for

estimating the position of blade cutting edge. Automation in Construction.106, 2019, 102890. DOI: https://doi.org/10.1016/j.autcon.2019.102890

12. Tavbay Khankelov. Results of experimental studies of the process of sorting of elastic components of municipal solid waste. Academic Journal of Manufacturing Engineering,volume19, ISSUE 4/2021, pp.97-102. DOI: https://ajme.ro/PDF_AJME2021 4/L14.pdf

13. R.Navon, E. Goldschmidt, Y. Shpatnisky. A consept proving prototype of automated earthmoving control.Automation in Construction.Volume 13, Issue 2, pp.225-239. DOI: https://doi.org/10.1016/j.autcon.2003.08.002

14. Fernando A., Auat Cheein,Jose Guivant. SLAM-based incremental convex hull processing approach for treetop volume estimation. Computers and Electronics in Agriculture.Volume 102, 2014,pp.19-30. DOI: https://doi.org/10.1016/j.compag.2014.01.002

TOSHKENT DAVLAT TRANSPORT UNIVERSITETI
Tashkent state transport university
International Journal Of Transport And Technological Machines
Tashkent 2025, issue 2, https://ijttm.uz/

ANALYSIS OF THE OPERATIONAL CHARACTERISTICS OF ENGINE OILS IN GASIFIED DIESEL ENGINES

Bakhytzhan Kedelbaev[1], Dmitriy Ayrapetov [2], Ismailov Ergash[2,]

[1]M. Auezov South Kazakhstan State University

[2]Tashkent State Transport University, Tashkent, Uzbekistan

Abstract: This study examines the changes in kinematic viscosity and flash point of engine oils during the operation of gasified diesel engines in buses. An analysis of the operational characteristics of oils used in transport companies was conducted, including LUKOIL Avangard Ultra M1 15W-40, TOTAL RUBIA WORKS 1000 15W-40, KV-G 15W-40, and Olympia Performance Top Trans Engine Oil 15W-40. During the research, oil samples were collected from ISUZU NP37 bus engines at different stages of operation (from 0 to 10,000 km mileage). Kinematic viscosity at 40°C and 100°C, as well as the flash point in a closed cup according to GOST 6356-75, were measured. The scientific novelty of the study lies in obtaining new experimental data on the degradation of engine oils under the operating conditions of gasified diesel engines. The research findings can be used to optimize oil change intervals and improve the reliability of vehicle power plants.

Keywords: Gasified diesel engines, engine oil, kinematic viscosity, flash point, thermo-oxidative stability, analysis of operational characteristics, mileage.

Introduction.

One of the key challenges in the economic and technological development of Uzbekistan is improving the reliability, economic efficiency, and environmental safety of motor vehicles, as well as reducing their material consumption and energy costs [1]. The quality of operational materials, including fuels, oils, and lubricants, along with their rational use, plays a significant role in addressing this issue [2,3]. Optimal engine oil replacement intervals directly impact the reliability of internal combustion engines (ICE) and the economic efficiency of transport and technological processes [4,5].

In recent years, the concept of considering lubricating oils as an integral part of engine design has gained increasing recognition. Understanding the patterns of changes in engine oil performance characteristics allows for more rational use in engines and provides a scientific basis for determining replacement intervals. Special attention is given to the operating conditions of oils in engines running in highly dusty environments. Determining the optimal oil replacement intervals remains one of the key and most complex tasks in fuel and lubricants science, requiring in-depth research under real operating conditions.

The physicochemical properties of used oil can serve as a diagnostic parameter, enabling an assessment of not only the current condition of the engine without disassembly but also predicting its continued reliable operation for a specified period.

Among the most significant operational indicators of engine oil, kinematic viscosity and flash point stand out, as they determine its functional properties. Kinematic viscosity is the ratio of dynamic viscosity to oil density at the same temperature. This parameter affects oil supply to the clearances of key friction units in the engine (cylinder-piston group, crankshaft), the formation of a hydrodynamic friction regime, ease of engine startup at low temperatures, mechanical losses, fuel efficiency, and the intensity of component wear [6–9].

To assess the service life of engine oil in internal combustion engines, some researchers propose using threshold values of operational characteristics, upon reaching which the oil should be replaced [8, 9, 10]. In particular, wear criteria include changes in flash point and kinematic viscosity: an increase in the latter by 25% or a decrease from the initial value by more than 20%.

Operating conditions of motor vehicles can vary significantly. Engine component wear, disruptions in the thermal operating regime, and other factors accelerate the degradation of engine oil properties [11]. This necessitates a revision of the manufacturer-specified oil change intervals. Delayed oil replacement can lead to an increase in the volume of used petroleum products, higher emissions of harmful substances, and, consequently, environmental degradation [12,13]. In this regard, studying the dynamics of kinematic viscosity changes at 40°C and 100°C, as well as the flash point of engine oils, is relevant for refining optimal replacement intervals [14,15].

The flash point of engine oil serves as an indicator of the presence of distillate fuel fractions. It changes due to unburned fuel ingress or leakage. For used oils, the critical flash point range is considered to be 170–180°C, while for high-viscosity oils, a decrease of 40–50°C is considered the limit. For example, if the oil contains 1% gasoline, the flash point drops from 200°C to 170°C, and at 6% gasoline, this value nearly halves. Fuel dilution of oil significantly deteriorates its anti-wear properties, accelerates the formation of carbon deposits and varnish on piston surfaces, and negatively impacts engine lifespan [16].

Materials and methods.

The research was conducted on gasified diesel internal combustion engines operating under commercial transport conditions. The objects of analysis were engine oils of the brands LUKOIL Avangard Ultra M1 15W-40, TOTAL RUBIA WORKS 1000 15W-40, and KV-G 15W-40, which are used in the company’s buses. The selection of these engine oils was based on their widespread use within the enterprise, as well as the necessity of studying their operational characteristics in gasified diesel engines. Olympia Performance Top Trans Engine Oil 15W-40

was considered as an alternative option; however, at the time of the study, it was not used in a specific bus.

The kinematic viscosity of the engine oil was studied in accordance with the requirements outlined in GOST 33-2016 “Petroleum Products. Determination of Kinematic Viscosity and Calculation of Dynamic Viscosity.” The essence of the kinematic viscosity determination method involved measuring the outflow time of a specified volume of engine oil under the influence of gravity at a constant temperature using a combined glass viscometer VPZh-2 with a capillary diameter of 1.31 mm.

A thermostat was used for heating and maintaining the required test temperatures (40°C and 100°C).

The kinematic viscosity of the engine oil was determined using the following formula:

$$\nu = c * \tau$$

where:

c — calibration constant of the viscometer, mm^2/s^2 (for the VPZh-2 viscometer, c = 0.2759 mm^2/s^2);

τ — sample outflow time from the viscometer, s.

The flash point of the engine oil was determined in a closed cup according to GOST 6356-75 – "Petroleum Products. Method for Determining the Flash Point in a Pensky-Martens Closed Cup."

Results and discussions.

During the operation of the monitored vehicles, studies were conducted on samples of fresh, in-use, and used oil, with mileage recorded. To diagnose the condition of specific components and assemblies, an oil sample of 0.1 L was taken (Table 1).

The key physicochemical properties of engine oils were examined, including kinematic viscosity at 40°C and 100°C, as well as the flash point in a closed cup.

Table 1. Technical Parameters and Operating Conditions of the Studied Vehicles

№	*Vehicle Brand*	*License Plate Number*	*Year of Manufacture*	*Initial Mileage, km*	*Engine Oil Brand at Start of Operation*	*Sample Volume Collected, ml*	*Fuel Type*
	1	*2*	*3*	*4*	*5*	*6*	*10*
1	*ISUZU NP37*	*90 937 ABA*	*2015*	*693 200*	*LUKOIL AVANGARD ULTRA M1 15W-40*	*100*	*LNG*

2	*ISUZU NP37*	*90 937 ABA*	*2015*	*698200*	*LUKOIL AVANGARD ULTRA M1 15W-40*	*100*	*LNG*
3	*ISUZU NP37*	*90 937 ABA*	*2015*	*703 200*	*LUKOIL AVANGARD ULTRA M1 15W-40*	*100*	*LNG*
4	*ISUZU NP37*	*90 946 ABA*	*2015*	*654 150*	*LUKOIL AVANGARD ULTRA M1 15W-40*	*100*	*LNG*
5	*ISUZU NP37*	*90 946 ABA*	*2015*	*659 150*	*LUKOIL AVANGARD ULTRA M1 15W-40*	*100*	*LNG*
6	*ISUZU NP37*	*90 946 ABA*	*2015*	*664 150*	*LUKOIL AVANGARD ULTRA M1 15W-40*	*100*	*LNG*
7	*ISUZU NP37*	*90 953 ABA*	*2015*	*753 500*	*TOTAL RUBIA WORKS 1000 15W-40*	*100*	*LNG*
8	*ISUZU NP37*	*90 953 ABA*	*2015*	*758 500*	*TOTAL RUBIA WORKS 1000 15W-40*	*100*	*LNG*
9	*ISUZU NP37*	*90 953 ABA*	*2015*	*763 500*	*TOTAL RUBIA WORKS 1000 15W-40*	*100*	*LNG*
10	*ZK612 6HG*	-	*2024*	*6000*	*KV-G 15W-40*	*100*	*LNG*
11	-	-	-	-	*Olympia Perfomance Top Trans Engine Oil 15W-40*	*100*	

Olympia Performance Top Trans Engine Oil 15W-40 was selected as an alternative option for comparative analysis. However, at the time of the study, it was not used in a specific vehicle, so mileage data is unavailable. The measured viscosity and flash point values are provided to assess its potential suitability for operation in gasified diesel buses.

The bus using KV-G 15W-40 operates within the same company but differs from the primary group of studied vehicles. This oil is considered another alternative option for gasified diesel bus operation. In the future, it may be chosen for broader application, which is why its characteristics have been included in the comparative analysis. The mileage of this bus differs from the others, as its operation began later.

After collecting engine oil samples, experiments were conducted to determine its physicochemical properties. Specifically, kinematic viscosity was measured to assess the oil's

flow properties at different temperatures, and the flash point was determined to indicate its fire resistance and volatility (Table 2).

Table 2. Dynamics of Changes in Kinematic Viscosity and Flash Point of Engine Oils

№	*Engine Oil Brand at Start of Operation*	*Initial Mileage, km*	*Mileage on Used Oil, km*	*Fuel Type*	*Flash Point, ˚C*	*Kinematic Viscosity at 40˚C, mm²/s*	*Kinematic Viscosity at 100˚C, mm²/s*
	1	*2*	*3*	*4*	*5*	*6*	*7*
1	*LUKOIL AVANGARD ULTRA M1 15W-40*	*693 200*	*0*	*LNG*	*221*	*108,43*	*16*
2	*LUKOIL AVANGARD ULTRA M1 15W-40*	*698200*	*5 000*	*LNG*	*217*	*96,98*	*14,9*
3	*LUKOIL AVANGARD ULTRA M1 15W-40*	*703 200*	*10 000*	*LNG*	*213*	*85,52*	*13,795*
4	*LUKOIL AVANGARD ULTRA M1 15W-40*	*654 150*	*0*	*LNG*	*221*	*108,43*	*16*
5	*LUKOIL AVANGARD ULTRA M1 15W-40*	*659 150*	*5 000*	*LNG*	*218*	*94,88*	*14,3*
6	*LUKOIL AVANGARD ULTRA M1 15W-40*	*664 150*	*10 000*	*LNG*	*215*	*82,77*	*13,52*
7	*TOTAL RUBIA WORKS 1000 15W-40*	*753 500*	*0*	*LNG*	*225*	*103*	*14,9*
8	*TOTAL RUBIA WORKS 1000 15W-40*	*758 500*	*5 000*	*LNG*	*221*	*92,5*	*14,4*
9	*TOTAL RUBIA WORKS 1000 15W-40*	*763 500*	*10 000*	*LNG*	*218*	*83*	*14*
10	*KV-G 15W-40*	*6000*	*6000*	*LNG*	*235*	*102,08*	*12,7*
11	*Olympia Perfomance Top Trans Engine Oil 15W-40*	*-*	*0*		*220*	*94,081*	*15,73*

According to the data presented in the table, a consistent trend in the operational characteristics of engine oil during its use in engines can be observed. Specifically:

- The flash point of engine oils decreases with increasing mileage, which may indicate oil dilution by fuel or its thermo-oxidative degradation. For example, the flash point of LUKOIL Avangard Ultra M1 15W-40 decreased from 221°C to 213°C after 10,000 km, while for TOTAL RUBIA WORKS 1000 15W-40, a similar decline was observed from 225°C to 218°C.
- Kinematic viscosity at 40°C and 100°C also decreases over the course of operation. For LUKOIL Avangard Ultra M1 15W-40, viscosity at 40°C dropped from 108.43 mm²/s to 85.52 mm²/s after 10,000 km, representing a ~21% decrease. A similar reduction was observed for the other tested oils.
- KV-G 15W-40, used in another bus, exhibited the highest flash point (235°C) at 6,000 km, which may indicate superior thermal stability.
- Olympia Performance Top Trans Engine Oil 15W-40 has not yet been used in a specific vehicle, but its physicochemical characteristics were included in the analysis to evaluate its potential for future use.

Thus, the obtained results confirm the necessity of monitoring the operational characteristics of engine oil as it is used in the engine. Further research will focus on analyzing oil thermal stability and improving its energy-saving properties through the development and introduction of new viscosity modifiers and antioxidant additives.

Conclusions and Recommendation.

As a result of the conducted research, changes in the kinematic viscosity and flash point of engine oils during their operation in gasified diesel buses were studied. It was established that as mileage increases, there is a consistent decrease in the flash point and a reduction in kinematic viscosity, which may indicate thermo-oxidative degradation of the oil and potential fuel ingress into the lubrication system.

Recommendations:

- To extend the service life of engine oil in gasified diesel engines, it is recommended to use oils with enhanced thermo-oxidative stability and low sulfate ash content.
- The optimization of oil change intervals should consider not only mileage but also operating conditions (temperature loads, fuel type, engine operating mode).

- To prevent oil dilution by fuel and loss of lubricating properties, it is advisable to conduct regular monitoring of kinematic viscosity and flash point, as well as to implement fuel content analysis in used oil.

Future Research Directions:

Future studies will focus on investigating the thermal stability of oils in gasified diesel engine operation. Special attention will be given to the development and introduction of new viscosity and functional additives that enhance the thermo-oxidative stability of oils and improve their energy-saving properties. This will not only extend the service life of engine oil but also increase overall engine efficiency, reducing mechanical losses and fuel consumption.

References

1. Decree of the President of the Republic of Uzbekistan "On Additional Measures for the Accelerated Development of the Automotive Industry of the Republic of Uzbekistan" No. PP-4397 dated 18.07.2019 // National Legislative Database, 19.07.2019, No. 07/19/4397/3449; 31.12.2020, No. 07/20/4938/1680. (in Uzbek)
2. Hakimov, R., Ayrapetov, D. Regeneration of spent low-freezing liquids AIP Conference Proceedings, 2024, 3045(1), 030064
3. Khakimov, R., Ayrapetov, D. Anti-corrosion coatings for the protection of metal parts of transport equipment AIP Conference Proceedings , 2024, 3045(1), 030065
4. Grigorov, A., Bondarenko, S., Khrystych, V., Maliarov, M., Maksymovska, N. Determination of Replacement Terms of Mineral Motor Oils Based on to their Actual Condition Petroleum and Coal, 2025, 67(1), страницы 16–23
5. Gołębiowski, W., Wolak, A., Šarkan, B. Engine Oil Degradation in the Real-World Bus Fleet Test Based on Two Consecutive Operational Intervals (2024) Lubricants, 12 (3), art. no. 101.
6. Impact of Vehicle Operating Conditions on Engine Oil Service Life / I. I. Shirlin [et al.] // Bulletin of the Siberian State Automobile and Road Academy. — 2013. — Issue 4 (32). — Pp. 42–45. (in Russian)
7. Investigation of Temperature-Viscosity Characteristics of Semi-Synthetic Engine Oils Used in Diesel Engines of Motor Vehicles / A. A. Pivovarchik, A. I. Sergei // Bulletin of Grodno State University named after Y. Kupala. Series 6: Engineering. — 2019. — Vol. 9, No. 1. — Pp. 78–87. (in Russian)

8. Physicochemical Quality Indicators of Engine Oil / E. D. Shpak, V. I. Mitrofanova // Bulletin of Amur State University. Series: Natural and Economic Sciences. — 2019. — No. 85. — Pp. 103–106. (in Russian)
9. Ensuring the Rational Service Life of Engine Oil in Engines / L. A. Dolgova, V. V. Salmin // Bulletin of Chuvash State Pedagogical University named after I. Ya. Yakovlev. — 2012. — No. 2 (74). — Pp. 146–156. (in Russian)
10. Investigation of Performance Indicators of Synthetic Engine Oils Used in Gasoline Engines of Passenger Cars / A. A. Pivovarchik, A. K. Gavrilenya, A. S. Korolkov // Bulletin of Baranovichi State University. Series: Technical Sciences. – 2022. – No. 1(11). – Pp. 37–42. – EDN EWQNZI.Rammohan, A. Engine's lubrication oil degradation reasons and detection methods: A review (2016) Journal of Chemical and Pharmaceutical Sciences, 9 (4), pp. 3363-3366. (in Russian)
11. Rammohan, A. Engine's lubrication oil degradation reasons and detection methods: A review (2016) Journal of Chemical and Pharmaceutical Sciences, 9 (4), pp. 3363-3366.
12. Ayrapetov, D. Technology development for producing plastic lubricant with secondary raw materials E3S Web of Conferences , 2024, 587, 01018
13. Akhmatjanov, R.N., Ismailov, E.U. Operation of vehicles in climatic conditions of Uzbekistan and their impact on ecology International Conference on Thermal Engineering, 2024, 1(1)
14. Investigation of the Operational Characteristics of Synthetic Engine Oils Used in Gasoline Engines of Passenger Vehicles / A. A. Pivovarchik, A. S. Korolkov, N. N. Alifirovets // Bulletin of Grodno State University named after Y. Kupala. Series 6: Engineering. — 2021. — Vol. 11, No. 2. — Pp. 21–27. (in Russian)
15. Investigation of the Operational Properties of Semi-Synthetic Engine Oils Used in Internal Combustion Engines of Volkswagen Polo Sedan Passenger Cars / A. A. Pivovarchik, O. D. Zabolotny // Bulletin of Grodno State University named after Y. Kupala. Series 6: Engineering. — 2021. — Vol. 11, No. 1. — Pp. 25–33. (in Russian)
16. Research on the Quality of Oils in Dump Trucks Operating in the Engines of Quarry Equipment in the Republic of Uzbekistan / Zebo Khamidullayevna Alimova // Mechanics and Technology. 2024. No. 17. URL: https://cyberleninka.ru/article/n/issledovaniya-kachestva-masel-avtosamosvalov-rabotayuschih-v-dvigatelyah-kariernoy-tehniki-respubliki-uzbekistan (in Russian)

TOSHKENT DAVLAT TRANSPORT UNIVERSITETI
Tashkent state transport university
International Journal Of Transport And Technological Machines
Tashkent 2025, issue 2, https://ijttm.uz/

EXPERIMENTAL EVALUATION OF THE THERMAL EFFICIENCY OF A MOBILE WATER DESALINATION DEVICE

Tursunov M. N., Sabirov H., Axtamov T. Z., Sh. A. Abriyev[1]

[1]Academy of Sciences of the Republic of Uzbekistan, Institute of Physical – Technical named after S.A. Azimov

Abstract: Thermal collectors form the basis of devices that use solar energy to convert mineralized saline water into drinking water. In this study, the thermal efficiency of a mobile water desalination device's thermal collector was investigated. The article analyzes the processes of increasing the intensity of solar radiation, directing it onto the surface of the thermal collector, the absorption of the directed solar radiation by the structure of solar elements, and the transfer and loss of thermal energy during the heating and evaporation of mineralized water. The experiments considered the effects of varying solar radiation intensity on the temperature changes of the water in the thermal collector and its influence on collector parameters. Based on the results, optimal design solutions were proposed to improve the thermal efficiency of the collector. This research supports the development of effective methods for utilizing solar energy to improve clean drinking water supply in rural areas, remote regions, and during emergency situations.

Keywords: Solar radiation, solar element structure, reflector, thermal collector, cooling system, short-circuit current, open-circuit voltage, solar radiation flux density.

Introduction.

Water covers approximately 67% of the Earth's surface. However, about 97% of this water is saline and unsuitable for drinking and irrigation, primarily located in oceans. Freshwater constitutes only about 3% of the planet's total water supply. Of this 3%, rivers and lakes account for merely 0.3%, while the rest is stored in underground aquifers and glaciers. Groundwater cannot serve as a permanent solution for consumption needs, as it is limited and the depletion of groundwater can harm ecosystems and existing infrastructure [1]. Because a large proportion of surface water is saline, water scarcity is a significant problem in remote areas of the world, especially in rural regions. If these areas have access to solar energy, solar-powered desalination systems can offer an alternative and efficient solution to overcome water scarcity. The growing global population and the expanding demands of industry and agriculture are intensifying the need for sustainable use of river, lake, and groundwater resources. However, these natural water sources are not always directly suitable for consumption, as they often contain excessive amounts of salts, various impurities, and microorganisms harmful to human health [2]. As a result, the process of desalinating saline water using solar energy can be considered a viable option for improving drinking water supply in saline regions. New technologies utilizing solar energy especially affordable, portable, and environmentally friendly desalination devices—could

play a critical role in addressing the global water supply problem in the future. For reference, drinking water consumption has increased sixfold over the past century, and according to research by experts and industry specialists, it is expected to double again by 2050. Currently, access to drinking water is a global economic issue, and its growing scarcity is caused by several factors, including:

- Rapid population growth leading to increased water consumption and the accelerated development of economic sectors that require significant water resources;
- Depletion of freshwater reserves due to overuse and the reduction of river flows;
- Pollution of water bodies by industrial and domestic wastewater, resulting in the loss of a portion of water from the freshwater reserves.

In the future, several additional possibilities exist for securing freshwater supply, including:

- Utilization of groundwater resources;
- Extraction of water from glaciers;
- Desalination of ocean and sea water;
- Collection and use of rainwater [3].
- Access to clean drinking water is one of the crucial factors for human health, and its adequate provision is directly linked to socio-economic development.

Desalination of mineralized water is a technological process aimed at reducing or completely removing dissolved salts and other contaminant components from the water. Seawater and ocean water contain a variety of dissolved substances, primarily mineral salts (mainly sodium chloride), gases (such as nitrogen, oxygen, carbon dioxide, and hydrogen sulfide), as well as trace amounts of organic compounds. Typically, the average salinity of ocean and sea water is about 3.47%, although this figure can vary between 3.4% and 3.6% depending on regional and climatic factors. In contrast, according to the World Health Organization (WHO) guidelines, the total dissolved salt content in potable water should not exceed 0.05% (500 mg/L) [4]. The desalination process is not limited to simply reducing salt concentration; it also requires the significant removal of other potentially harmful components from the water. These include ions such as calcium, magnesium, sulfate, nitrate, heavy metals, as well as microbiological contaminants that may pose risks to human health.

Comparative analysis of seawater composition and drinking water. Table 1.

Water type	**Salt content (%)**	**Mineral salts (mg/l)**	**Potability**
Ocean water	3,47	34,700	Invalid
Sea water	3,4-3,6	34,000-36,000	Invalid
Drinking water	≤ 0,05	≤ 500	Valid (WHO standard)

Structure of the water desalination device

The water desalination device based on a solar cell structure is designed to extract clean water from saline sources, either for drinking purposes or for other technical applications. The primary energy source for the operation of the device is solar radiation. This device features a simple construction, requires relatively low economic investment, and demands minimal additional maintenance.



Figure 1. Front view of the mobile solar-powered water desalination device

The thermal collector (TC) of this device is made from a stainless steel-based metal alloy, providing high resistance to corrosion in saline water environments. The external surface of the collector (the side facing the sun) is thermally insulated from radiation. Inside the TC, a structure composed of crystalline silicon solar cells with a power rating of 150 W is installed, efficiently absorbing the incoming solar radiation. Along the arrangement of the solar cell structure inside the TC, there is a special slit designed to facilitate the free movement of the generated water vapor.

Connected to this slit is a cooling system that reduces the temperature of the vapor, causing condensation to occur. Water droplets form due to gravity and are collected into a reservoir located at the bottom of the system. Reflectors (flat mirror-like surfaces) positioned on both sides of the thermal collector can enhance the intensity of the incoming solar radiation by up to two times.

The mobile cart structure of the device also includes an adjustable handle for setting the optimal tilt angle, along with storage tanks for the saline feedwater and the produced clean water.

The transparent tempered glass cover allows solar radiation to pass through and concentrate it onto the surface of the solar cell structure, ensuring high absorption. This increases the temperature of the mineralized water and raises the overall temperature of the thermal collector, actively initiating the evaporation process. The generated water vapor rises inside the TC, reaches the internal surfaces connected to the cooling system, moves towards the slit, and under conditions of a temperature lower than the ambient environment, condenses to form droplets. These droplets are then collected as fresh water in a special storage container [5, 6, 7].

Testing Procedure: The water desalination device developed based on the solar cell structure was set into operating mode at an average optimal tilt angle of $\alpha = 38–39°$ relative to the horizon (corresponding to the last five days of March). During the experiment, the position of the device was adjusted hourly to ensure that the solar radiation was directed as perpendicularly as possible to the surface of the thermal collector (TC). The tests were conducted daily from 10:00 AM to 4:00 PM during sunny days in February and March.

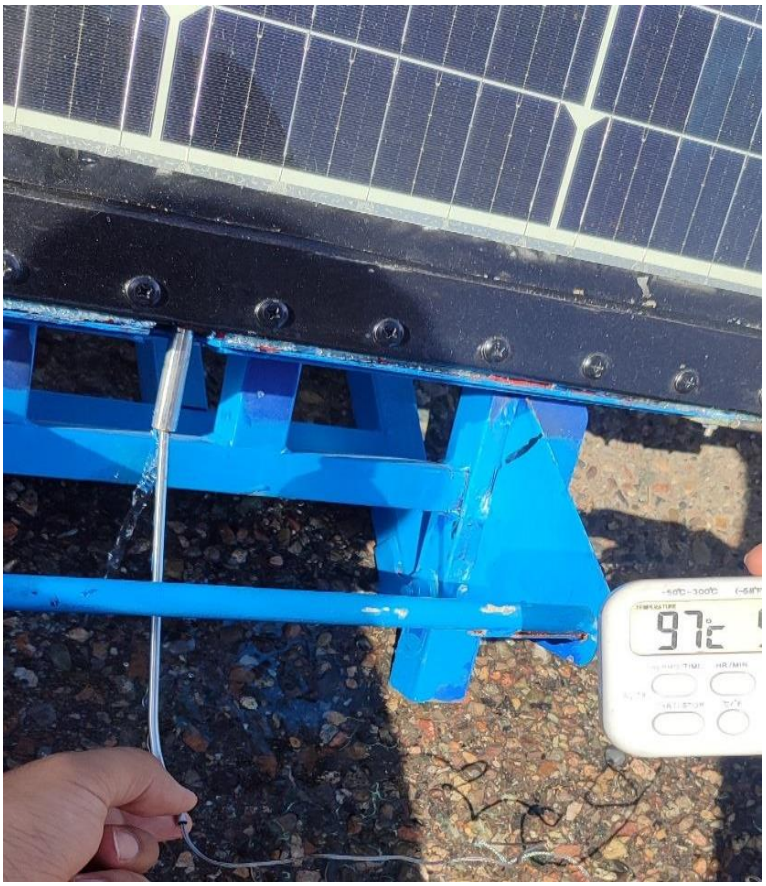


Figure 2. Shows the measurement of the water temperature inside the TC during the experiment

In the initial stage, the TC's frontal surface, filled with saline water, was directly exposed to solar radiation. To rapidly increase the water temperature, two side reflectors and one bottom reflector were integrated into the device design. These reflectors significantly increased the concentration of thermal energy by redirecting the solar radiation flux density onto the TC surface.

As a result, the heat energy generated by the solar cell structure installed inside the TC led to a rapid rise in the temperature of the saline water. Experimental results showed that the temperature of the saline water, initially at 14°C, rose to 97°C within just one hour under focused solar radiation through the reflectors.

This outcome demonstrates that the reflectors, by enhancing the intensity of solar radiation by approximately 1,5–1,8 times, effectively intensified the thermal flux and significantly improved the operational efficiency of the desalination device.

Results and discussion. The experimental work for this study was conducted during February–March 2025 under sunny weather conditions at the Heliopolygon of the Institute of Physics and Technology in Tashkent. During the tests, the newly designed water desalination device was evaluated. The thermal collector of the device has a capacity of 16 liters.

At the beginning of the experiments, the initial temperature of the saline water was recorded at 14°C, while the ambient temperature was measured at 18°C.

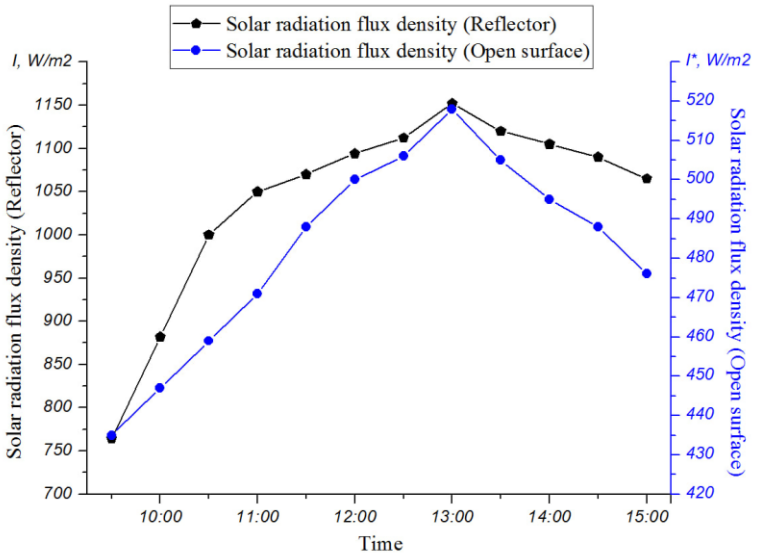


Figure 3. Time-dependent variation of the measured values of SRFD falling on the front surface of the water purifier

Figure 3 illustrates the variations of solar radiation flux density (SRFD) over time, showing both its high and low values. Solar radiation is influenced by several main factors: atmospheric effects, geographical location, temporal variations, and solar activity [8, 9]. To enhance the SRFD during spring days, side reflectors were utilized.

On March 19, 2025, under conditions of relatively low solar radiation intensity, the SRFD measured without reflectors at 10:00 am was 415 W/m². At the same time, by employing side reflectors, the SRFD value almost doubled, reaching 825 W/m². The maximum radiation intensity was observed at 1:30 pm; at that time, the SRFD measured without reflectors was 550 W/m², while with the help of side reflectors, it increased to 1,135 W/m².

Such high SRFD values can reach up to 1,600 W/m² or even higher during the summer months, suggesting the feasibility of expanding the utilization of this energy. For this purpose, the solar cell structure placed inside the thermal collector served a dual role: it functioned both as a blackbody absorber for thermal energy and as a photovoltaic cell for generating electrical energy.

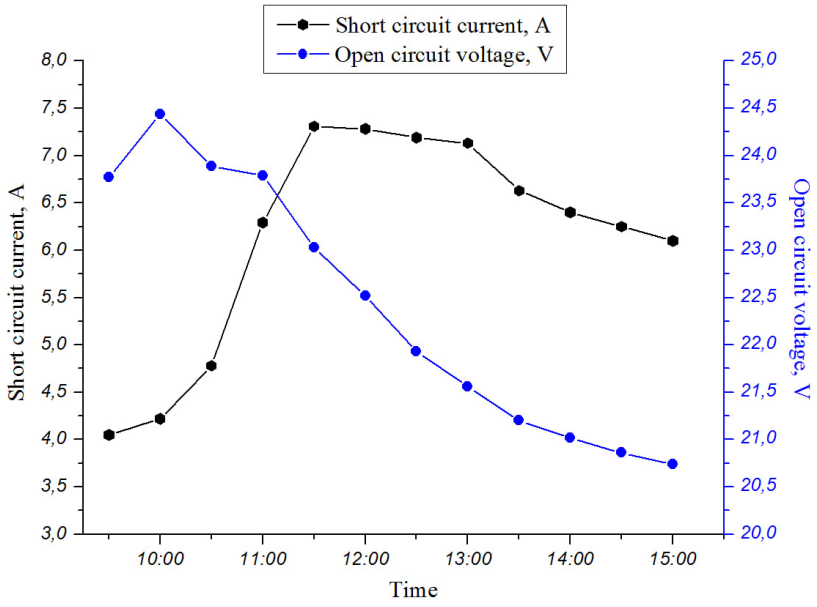


Figure 4. The time-dependent changes in the desalination plant (OCV and SCC) during high and low solar radiation flux density (SRFD) days are shown

The following graph illustrates the time-dependent variations of the Open-Circuit Voltage (OCV) and Short-Circuit Current (SCC) based on hourly changes.

During the experiment, at 9:30 AM, the OCV was recorded at 23,5 V, and by 9:50 AM, it reached its peak value of 24,6 V. This phenomenon can be explained by the very low initial

water temperature inside the collector. Over time, as the intensity of solar radiation naturally increased, the water temperature within the collector gradually rose, leading to a decrease in the OCV down to 20,7 V.

As the temperature rises, the internal characteristics of the semiconductor material change, causing a reduction in the open-circuit voltage [10]. This relationship can be expressed by the following formula:

$$V_{oc} = \frac{kT}{q} ln(\frac{I_L}{I_O} + 1)$$

Where, k– Boltsman constant ($1{,}38 \cdot 10^{-23}$ J/K), T – Absolute temperature (Kelvin), q – Electronic charge ($1{,}6 \cdot 10^{-19}$ C), I_L– The current generated under the influence of light, I_o – recombination current.

The short-circuit current (V_{oc}) primarily depends on the intensity of solar radiation, while the effect of temperature on it is comparatively minor. At 9:30 am, the initial measured point indicated a current of 4,1 A. As time progressed, due to the natural increase in solar radiation flux density (SRFD), the short-circuit current (V_{oc}) also rose. The direct proportional relationship between SRFD and I_{sc} is confirmed by Equation (2):

$$I_{sc} = qGLW(1 - R)$$

Where, q — elementary charge ($1{,}602 \cdot 10^{-19}$ C), G — generation rate (light absorption intensity), L — diffusion length of charge carriers, W — width of the active region, R — reflection coefficient of solar radiation.

The increase in the temperature of the saline water significantly affects the open-circuit voltage (V_{sc}), whereas the short-circuit current (I_{sc}) remains almost unchanged or only slightly decreases. Research results show that for every 1°C increase in temperature, I_{sc} changes by only about 0,03% to 0,1% [11].

The total surface area of the device is 7,668 cm². During the spring season, the solar-powered water desalination device produced 10–12 liters of potable water per day (over a period of 6 hours), which corresponds to more than 1,6–2 liters of clean drinking water per hour. The device is capable of effectively purifying not only seawater but also brackish and contaminated waters from rivers and sewage systems.

This solar desalination device efficiently removes key dissolved particles, including salts and minerals such as sodium (Na^+) and calcium (Ca^{2+}). By utilizing solar energy, the device

heats saline water and initiates the evaporation process within approximately 35 minutes. The generated water vapor then passes into a special cooling system, where it condenses over a period of about 47 minutes, collecting as clean water droplets in a designated storage container.

The efficiency of a solar thermal collector system is an important parameter that indicates the proportion of incident solar radiation effectively utilized as useful heat for water evaporation. This efficiency can be determined using the following formula.

$$\eta = \frac{Q_u}{Q_t} \times 100\%$$

Where, η -thermal efficiency (%), Q_{useful} - useful thermal energy consumed for water evaporation (J), Q_{total} - total incident solar energy on the collector surface (J).

The thermal energy used for water evaporation is calculated as.

$$Q_u = r \cdot m$$

Where, r- latent heat of vaporization of water (kJ/kg), typically r=2,423,300 J/kg, m- ass of evaporated water (kg), here m=0,5 kg.

The total solar energy input is determined by:

$$Q_t = E \cdot S \cdot \Delta\tau$$

Where, E- solar radiation intensity (W/m^2), E=950 W/m^2, S- collector surface area (m^2), S=0,7668 m^2, Δτ-duration of solar exposure (s), τ=10,800 s.

Final calculation: $Q_u = 2,423,300 \cdot 0,5 = 1,211,650$ J,

$Q_t = 950 \cdot 0,7668 \cdot 10,800 = 7,867,368$ J.

$$\eta = \frac{Q_u}{Q_t} = \frac{r \times m}{E \times S \times \tau} = \frac{1211650}{7867368} \times 100\% = 15.4\%$$

Conclusion. The conducted experimental studies demonstrated that the portable solar-powered water desalination device is environmentally friendly, economically efficient, and characterized by high energy efficiency. The installation of reflectors on the device's thermal collector significantly increased the solar radiation flux density, allowing the saline water temperature to reach 97°C within 2–3 hours. Moreover, the analysis of the electrical parameters of the solar cells revealed their dependence on temperature and solar radiation intensity. On average, the device was able to produce up to 0,5 liters of clean drinking water per hour.

Additionally, this system can be successfully employed to obtain potable water from seawater, river water, and wastewater sources. The device presents a particularly promising solution for remote areas where centralized water supply infrastructure is not available.

This study constitutes a component of an ongoing scientific research project and is based on experimental investigations that have not yet reached their final stage. At each phase, the system's efficiency, operational performance, and design solutions are analyzed separately based on new modifications of the experimental setup. In the upcoming experimental models, special attention is being given to minimizing the impact of energy losses and identifying factors that enhance the system’s overall efficiency. The ultimate goal is to improve the device’s performance and develop an energy-efficient and cost-effective technology.

References

1. Ahsan A, Islam KMS, Fukuhara T, Ghazali AH. Experimental study on evaporation, condensation and production of a new Tubular Solar Still. Desalination. Vol 260, Pp. 172–179. 2010.
2. Salman H. Hammadi, Dhafer Manea H. Al-Shamkhee, Hussein Ali Jabar. International journal of energy and environment. Vol 6, Issue 6, Pp 587-596.
3. L. Garcia-Rodriguez. Seawater desalination driven by renewable energies: A review. Desalination. Vol. 143. №2. 2002. Pp. 103–113. DOI: 10.1016/S0011-9164(02)00232-1.
4. A. Madhlopa, C. Johnstone. Potential for water distillation by using solar energy in Malawi. Environment and Health International. Vol 10, issue 2, Pp. 51. 2008.
5. Muminov R. Tursunov M. Yuldoshev I., Sabirov H., Kholov U.R., Axtamov T.Z. Features of optimization of increasing the efficiency of an autonomous photo thermal installation for rural regions. E3S Web of Conferences. 216(72):01146 (2020). RSES 2020. DOI:10.1051/e3sconf/202021601146.
6. M.N. Tursunov, X. Sabirov, T.Z. Axtamov Sh.A. Abriyev. Разработка нового метода полученияпитьевой воды из минерализованных источников Scientific Journal of Mechanics and Technology: Vol 5, issue 3, 2024.
7. M.N. Tursunov, X. Sabirov, Sh.A. Abriyev, T.Z. Axtamov, Y.M. Qurbanov: Testing a mineralized water desalination device using solar energy in winter conditions, “Energy innovatsions: fundamentals and innovative engineering sollutions”. Pp. 1150-1153. 2025.
8. Islom Jurayev, Isroil Yuldoshev and Zukhra Jurayeva. Results of Study of Photovoltaic Thermal Battery Based on Thin-Film Module by Modeling and Computational Methods. //

Proceedings of International Conference on Applied Innovation in IT. Volume 12. Issue 1. Pp. 243-249. 2024. DOI:10.25673/115707.

9. Green, M. A. (1982). Solar Cells: Operating Principles, Technology, and System Applications. Prentice Hall. https://www.worldcat.org/title/solar-cells-operating-principles-technology-and-system-applications/oclc/8785149
10. Gueymard, C. The sun's total and spectral irradiance for solar energy applications and solar radiation models. Solar Energy. 2004. https://doi.org/10.1016/j.solener.2003.08.039.
11. M.N. Tursunov, H. Sabirov, T.Z. Axtamov, M. Tursunov, M. Chariyev, H. Abdullayev. *Creation of all-season photothermal installation of increased efficiency.* "Proceedings of the 11th International Conference on Applied Innovations in IT". Volume 11. Issue 2. Pp. 125-131. 2023. DOI:10.25673/113002.